Analytical and numerical investigation of unsteady wind for enhanced energy capture in a fluctuating free-stream

David Wafula Wekesa [a], [*], Cong Wang [b], Yingjie Wei [b], Louis Angelo M. Danao [c]

[a] *Department of Physics, Machakos University, Machakos County, Machakos, Kenya*
[b] *Department of Aerospace Engineering and Mechanics, School of Astronautics, Harbin Institute of Technology, Harbin City, PR China*
[c] *Department of Mechanical Engineering, University of the Philippines, Diliman, Quenzon City, Philippines*

ABSTRACT

Unsteady wind is characterized by low energy content and large fluctuations. A Computational Fluid Dynamics (CFD)-based method for capturing wind energy in a fluctuating free-stream, supported by analytical formulations, is investigated in this paper. We implemented unsteady Reynolds-Averaged Navier-Stokes (RANS) solver to control the dynamic mesh motion. Using an urban wind resource, characteristic fluctuation frequencies at 0.5 Hz, 1.0 Hz, and 2.0 Hz have been selected to demonstrate the enhanced wind energy capture. The numerical energy coefficient marginally changed from 0.36 at 0.5 Hz to 0.37 at both 1 Hz and 2 Hz cases. The results reveal that the highest frequency of fluctuation with meaningful energy content in unsteady wind condition is ≈ 1 Hz. The study findings promote our understanding about the energy associated with short-period fluctuations reflecting realistic unsteady wind environment. Additionally, the present study approach to analyze wind energy capture on a H-Darrieus wind rotor in a fluctuating free-stream can be extrapolated to other slightly complex VAWT configurations.

© 2017 Elsevier Ltd. All rights reserved.

1. Introduction

The driving force for the creation of winds, primarily in differences between the equator and the poles, has been attributed to uneven solar heating of the earth's surface [1,2]. The unsteady winds are associated with urban environment due to enhanced local roughness, and by virtue of their low location in the planetary boundary layer [1,3]. These results to complex, gusty, and shifting urban wind resource exhibited by relatively rapid changes in both wind direction and magnitude. In spite of wind turbines being the biggest rotating machines (up to 110 m diameter with their blade approximated to the size of the span of a Boeing 777), they operate in the planetary boundary layer [4]. The major field of science involved in the primary process of extracting this kinetic energy from the wind and conversion to mechanical energy at rotor axis is referred as aerodynamics [4,5].

The aerodynamic velocity field within the planetary boundary layer is notoriously complex with mean winds varying spatially and temporary with features such as shear, vortices, separated and reattached flows, and recirculating eddies [6—9]. In addition, steady wind is an off-design condition for wind turbines as opposed to most aircrafts which try to fly high enough to avoid turbulence and extreme wind events in the planetary boundary layer. This is because, for wind turbines, all aerodynamic phenomena are essentially unsteady.

The majority of the wind's kinetic energy is contained within the steady and long period components, resulting in relatively high mean wind speeds. In contrast, a surface with a large roughness, such as an urban wind environment, generates large shear stresses. These result in high levels of turbulent mixing leading to a dramatic increase in the level of fluctuations [10]. Numerical and wind tunnel experimental studies for unsteady wind rotor performance have been investigated and discussed in Refs. [3,11—22] to describe accurately their response to short-period micrometeorological fluctuations. However, from these studies, the approximation of the unsteady periodic wind for capturing wind energy was inconsistent due to the limited small range of fluctuation frequencies considered.

Performing wind tunnel or flight experiments in unsteady flows is limited by huge capital cost requirements, an array of diverse technical skills, time constraints, operational know-how, and a

* Corresponding author.
E-mail address: dwekesahit@gmail.com (D.W. Wekesa).

number of physical and environmental parameters that can influence measurements [22,25–31]. These limitations can be overcome by CFD numerical simulations as a result of continuous improvements in numerical methods as well as the development of speed and storage capability of computers [32,33]. Although much progress has been made for simulation methods like Direct Numerical Simulations (DNS) and Large-Eddy Simulations (LES) in the CFD community, these two methods are inappropriate and currently outside in the realm of industrial applications for Reynolds numbers typically found in external aerodynamics [34–36,38–42].

This paper is a continuation of the work reported by the authors in previous studies [21–24]. Based on analytical formulations (Section 2), in this paper, we seek to present unsteady Reynolds-Averaged Navier-Stokes (RANS) solver with a developed CFD-based 2D model to analyze wind energy capture on a 1.5 kW VAWT in a fluctuating free-stream. Additionally, unsteady calculations have been applied to demonstrate enhanced wind energy capture across a wide range of fluctuation frequencies for consistency.

2. Theoretical basis

Virtually all wind turbines operate in the lower 10% of the earth's planetary boundary layer in a region termed the internal sub-layer [2,3]. Unsteadiness within the internal sub-layer, characterized by amplitude fluctuations $u'(t)$ causes a departure of wind speeds away from the long term mean $\overline{u}$ to span a vast range of time scales ranging from months to seconds [21,22,43],

$$u(t) = \overline{u} + u'(t) , \tag{1}$$

where u is fluctuating wind as a function of time, t.

Moreover, an assessment of the wind resource can be analyzed out by splitting unsteady wind into three components [2]:

$$u(t) = \overline{u} + u'_{sp}(t) + u'_{lp}(t), \tag{2}$$

where $\overline{u}$ is overall mean wind speed, u'_{sp} is short period fluctuations in the order of seconds to minutes, and u'_{lp} is long period fluctuations in the order of 10–100 hours. The effects of long period fluctuations can be neglected without any loss of generality since the system response will be fast enough to follow the ideal operating point of the VAWT [14]. However, short period fluctuations close to the order of the VAWT rotational frequency will possibly affect the performance of the wind turbine because VAWT runs at constant rpm due to its inertia despite the change in condition. Hence, the present study focuses on the short period fluctuations.

McIntosh et al. [13] proposed a notation to describe unsteady wind variations experienced by a wind turbine rotor axis during a gust, expressed as:

$$D_g = \frac{U_{mean}}{f_c}, \tag{3}$$

where D_g is the gust length, U_{mean} is the mean free-stream velocity, and f_c is the characteristic fluctuation frequency of the gust. The gust-induced unsteady aerodynamic effects can then be characterised by a reduced gust frequency k_{gust} relating the rotor's radius R_{rotor} to the characteristic frequency f_c of the fluctuating wind, expressed as:

$$k_{gust} = \frac{2R_{rotor}}{D_g} = \frac{2R_{rotor}f_c}{U_{mean}}. \tag{4}$$

Following the notation by Wekesa et al. [21,22,37], the number of rotor revolutions per one full cycle of wind fluctuation, n_{rev}, can be expressed as:

$$n_{rev} = \frac{\lambda_{mean}}{\pi k_{gust}} = \frac{\lambda_{mean}U_{mean}}{2\pi R_{rotor}f_c} , \tag{5}$$

where the mean tip speed ratio $\lambda_{mean} = (\omega_{mean}R_{rotor})/U_{mean}$. In the present study, the simulation is such that one wind cycle is exactly 48, 24, and 12 full rotor cycles at $f_c = 0.5$ Hz, 1.0 Hz, and 2.0 Hz, respectively, at a constant rotor angular velocity $\omega = 149.29$ rad/s with machine's mean $\lambda_{mean} = 4.75$ (Table 3). The angular velocity was kept constant in order to isolate the aerodynamic effects that are introduced by the fluctuating wind speed from those that will be introduced additionally when the rotor accelerates or decelerates [21]. Total available wind energy E_{wind} over period of operation T can be calculated through an integration of available wind power using the expression [13,44]:

$$E_{wind} = \frac{1}{2}\rho A \int_0^T U_\infty^3(t)\mathrm{d}t , \tag{6}$$

where U_∞ is the free-stream wind velocity.

However, from Bertényi et al. [3] study, Eq. (6) is different from the energy estimate calculated by taking the cube of the average wind speed ($\frac{1}{2}\rho A\overline{u}^3 T$) indicating that the latter ignores the unsteady energy contribution. Therefore, when assessing potential turbine sites, a discretized form of Eq. (6) is preferred [13]:

$$E_{wind} = \frac{1}{2}\rho A \sum_{i=1}^{T/\Delta t} U_\infty^3(t)\Delta t , \tag{7}$$

where Δt is the time of interest. Furthermore, the unsteady power production for a turbine operating over the same time period can be integrated to give the total aerodynamic energy generation E_{turb} [13]:

$$E_{turb} = \frac{1}{2}\rho A \int_0^T CP(\lambda)U_\infty^3(t)\mathrm{d}t , \tag{8}$$

where CP is the power coefficient defined as the ratio of blade average power to wind average power. Consequently, the ratio of extracted aerodynamic energy to available wind energy over a pre-defined period of time yields the energy coefficient C_e [13]:

$$C_e = \frac{E_{turb}}{E_{wind}} = \frac{\int_0^T CP(\lambda)U_\infty^3\mathrm{d}t}{\int_0^T U_\infty^3\mathrm{d}t} , \tag{9}$$

where for an unsteady wind, CP is a function of λ evaluated over one fluctuation wind cycle (Eq. (5)). For a steady wind, C_e evaluated over a turbine revolution equals CP [2,13].

3. Numerical method

3.1. Computational model description

The flow solver used for the present study is the CFD code Fluent® that solves the unsteady, 2D and incompressible full unsteady RANS. This code uses the finite volume method to solve the governing equations for fluids [21–24,45]. The unsteady RANS

Table 1
Main geometric features of the tested three-bladed rotor blade.

Blade profile	Value	Unit
Blade airfoil	NACA 0022	
Number of blades	N = 3	[−]
Chord	c = 0.04	[m]
Solidity	σ = 0.34	[−]
Spoke-blade connection	0.25c	
Simulation	2D	

Table 2
Summary of the boundary conditions applied on the domain.

Boundaries in Fig. 2(a)	Boundary conditions in the solver
B1	Velocity inlet
B2, B3	No-slip wall
B4	Pressure outlet
B5	Interface

Table 3
Details of the numerical set-up and under-relaxation factors.

Description	Value	Unit
Air viscosity	1.8×10^{-5}	[kg/(m s)]
Air mass density	1.23	[kg/m^3]
Angular velocity	149.29	[rad/sec]
Free-stream wind velocity	11.00	[m/s]
Machine mean tip speed ratio	4.75	[−]
Under-relaxation factors		
Pressure	0.2	[−]
Density	1	[−]
Body forces	1	[−]
Momentum	0.7	[−]
Specific dissipation rate	0.8	[−]
Intermittency	0.8	[−]
Turbulent Viscosity	1	[−]

approach appears to be the most suitable to predict the aerodynamic performance simulations with an acceptable computational cost and give reasonable results [21–23,46–49]. The reader is referred to [22,50–58] for detailed descriptions about development of CFD methods and applying high-resolution for simulating unsteady aerodynamic flows. The airfoil coordinates of a NACA 0022 profile were imported to define the blade shape, as was the case in the blade thickness analysis study by Wekesa et al. [21]. The main rotor features are summarized in Table 1, where the solidity parameter is defined as suggested in Refs. [21,22,59,60]: σ = Nc/R$_{rotor}$.

3.2. Mesh and boundary conditions

The model geometry was created from the formatted data points in mesh generation software ANSYS® ICEM CFD™. A moving mesh approach with a sliding mesh technique was used for the rotation of the inner circular Rotor sub-grid zone in order to capture the torque generated by the three-bladed rotor [21–23].

A structured O-grid topology was generated where the size of the first cell height next to the wall (Fig. 2(b)) was limited by y$^+$ < 1 [61]. This was the limit of the turbulence model that was chosen for the simulations. The O-type mesh was primarily used in preference to conventional C-grid topology because the expected wake is not fixed on a specific path relative to the blade but rather varying greatly in direction swaying from one side to another side [11,21,22,62].

The appropriate number of nodes on the airfoil surface is among the main factors that influence the accuracy of the forces generated

on the blade surface [11]. Similar to the observations reported in the authors' previous work in Ref. [11], five surface node densities were tested at $\lambda = 2$ and $\lambda = 4$ where the blade torque for one blade in one full rotation were compared as shown in Fig. 1. A node density of 300 points is considered to be a reasonable number in so far as accuracy of the predicted torque is concerned. Therefore, for both low and high λ, a final node density was set to 300 points as this was seen to be the most appropriate density.

The boundary conditions applied at the boundaries shown in Fig. 2(a) are summarised in Table 2. The instantaneous inlet velocity Eq. (13) is used at the 'Velocity inlet' boundary. The computational domain consists of two mesh zones; the inner circular Rotor sub-grid zone and the rectangular outer zone, and they communicate via a pair of circular interfaces between them. The two mesh zones coincides exactly and their interface boundaries slide against each other with no excessive overlap to minimize numerical diffusion, and have approximately the same characteristic cell size in order to obtain faster convergence [11,21,22,46]. The rotation of the inner domain relative to the outer domain is prescribed within the flow solver that implements the algorithm for the sliding mesh. As alluded to earlier in Refs. [21,22,63], care was taken such that tolerance between meshes in the interface was kept low to avoid excessive numerical diffusion.

The inner Rotor sub-grid zone is composed of three symmetric airfoil blades rotating at a common angular velocity and spaced equally at 120° apart (Fig. 2(a)). The blades were defined as no-slip walls, while both interface boundary of the Rotor sub-grid and the outer rectangular wind tunnel sub-grid were set as an interface to ensure continuity in the flow field. The interface was defined by coupling the stationary domain with the rotating one [21,22].

To reduce computation time, the outer domain was coarsely meshed with a maximum edge length cell set to the length of the chord as shown in Fig. 3. This dissipated the high gradients in the wake, such as shed vortices, but the general velocity deficit was still captured [63]. In addition, since the pattern of the developed wave is not within the scope of the present study, the coarseness of the mesh in the stationary was not considered as an issue. Following the wall distance studies by Wekesa et al. [22] and Danao et al. [11], the side wall distance was set to 1.2 m rotor diameter from the VAWT axis (Fig. 2(a)) giving a blockage ratio of 0.29 which is equal to that of the actual wind tunnel setup [25]. The velocity inlet boundary condition was set to 1.8 m rotor diameter upwind, and the pressure outlet boundary condition was placed at 3 m rotor diameter downwind to match the actual distance of the wind tunnel fan from the VAWT rotor axis of rotation [21,22,25]. Following a downwind boundary study for the VAWT model in Ref. [11], an insignificant change in CP was revealed over a wide range of tip speed ratios from 1.2 m to 3.0 m. Thus, the pressure outlet boundary distance of 3 m was sufficient to ensure that the wake development by the VAWT was not terminated prematurely.

Following the authors' previous work in Refs. [11,21,22], turbulence intensity of inlet flow was set to Tu = 8% with a turbulence viscosity ratio of μ_t/μ = 14. As stated in Refs. [11,21,22], these conditions were selected to provide a matching turbulence intensity decay that was observed in Danao et al. [25,63] experiments. The experiments [25,63] were conducted using a hot-wire anemometer at 100 Hz, 1000 Hz, and 10,000 Hz to measure wind speeds in the wind tunnel. The hot-wire was calibrated using a micromanometer. The turbulence intensity was computed from the velocity fluctuations measured. As can be seen in Fig. 4, the modeled turbulence intensity decay in the simulations matched that of the experiments. Similar results were obtained in Ref. [11] with the numerical model matching the observed decay in the experiments. The reader is referred to [11,21,22,63–65], and
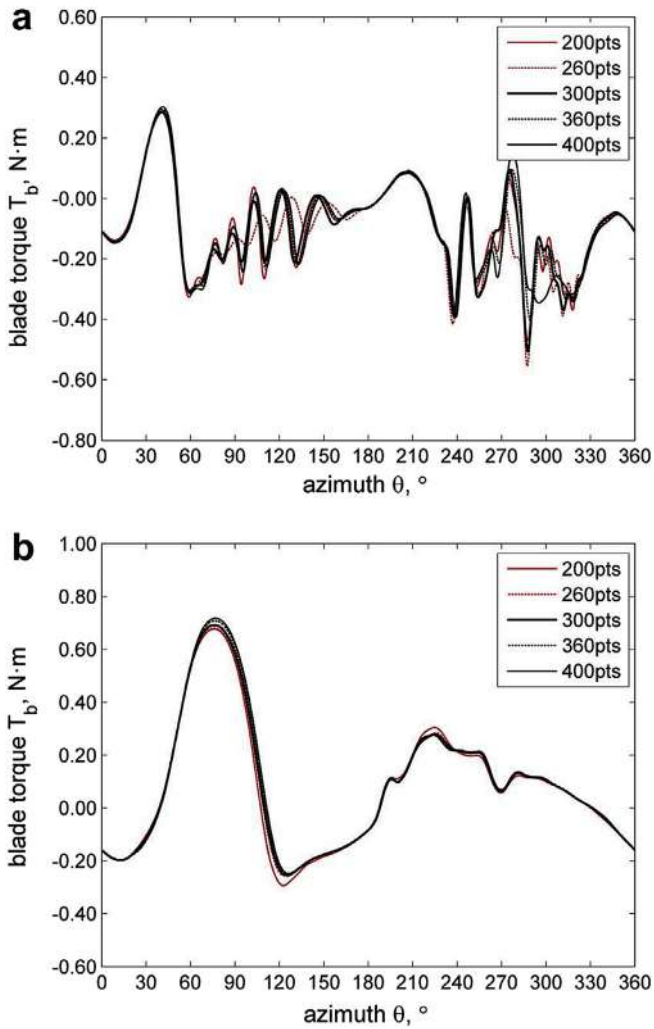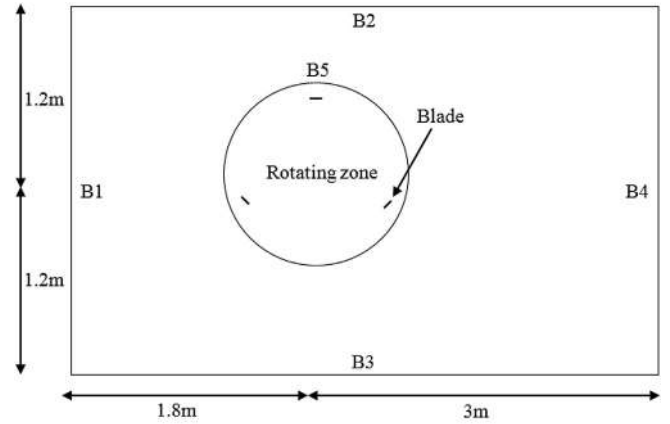
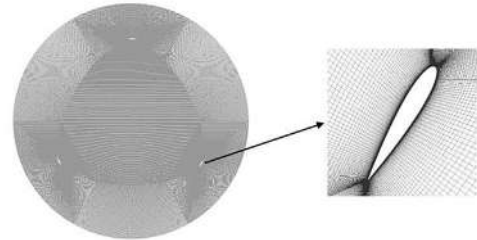Fig. 1. Blade torque for node density study: (a). $\lambda = 2$, and (b). $\lambda = 4$ [11].

(a) Boundary conditions of the Wind tunnel sub-grid

(b) Mesh adopted near the rotor blades

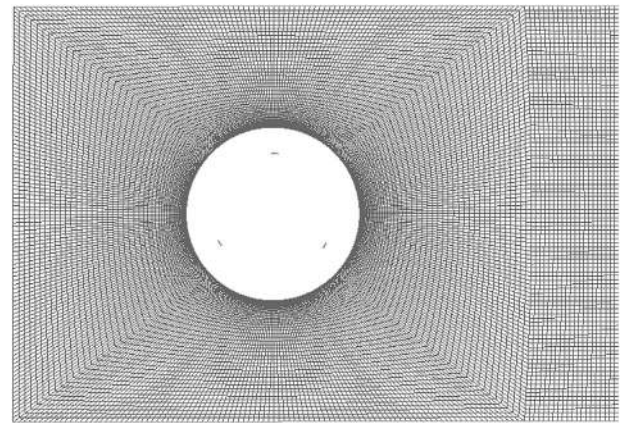Fig. 2. An illustration of boundary conditions and mesh adopted near the rotor blades.

Fig. 3. The stationary outer domain mesh of the numerical model.

references therein] for full details on domain boundary location with both mesh and time step independence preliminary studies.

3.3. Time step independence study

Sufficient temporal resolution is necessary to ensure proper unsteady simulation of the VAWT [11]. Different time step sizes Δt that are equivalent to specific rotational displacements along the azimuth have been tested by the authors in the previous work [11,37] as shown in Fig. 5. The largest Δt used was equal to a $\Delta t = 1^0 \omega^{-1}$ (time for one degree equivalent rotation) and was subsequently halved twice over to get $\Delta t = 0.5^0 \omega^{-1}$ and $\Delta t = 0.25^0 \omega^{-1}$. All three time step sizes were tested at $\lambda = 2$. It was appropriate to select the time step size at $\lambda = 2$ with converged solutions, so as to ensure convergence at higher tip speed ratio was achieved. Observe in Fig. 5 that, there is a delay in the torque ripple for the coarsest $\Delta t = 1^0 \omega^{-1}$ while the two finer time step sizes are in good agreement especially in the upwind. A small difference in predicted magnitude of T_b between $\Delta t = 0.5^0 \omega^{-1}$ and $\Delta t = 0.25^0 \omega^{-1}$ is seen from $\theta = 280^0$ to $\theta = 330^0$ but the peaks and troughs are still in synchronization. Therefore, a chosen time step size at $\Delta t = 0.5^0 \omega^{-1}$ was adopted for accurate simulations for the remaining runs.

3.4. Modelling of wind velocity fluctuations

To model a fully developed unsteady wind inflow in the virtual wind tunnel, appropriate velocity profiles are applied at the inlet boundary (Fig. 2(a)). The wind velocity fluctuations can be idealized with a mean value, an amplitude, and a frequency using a stochastic differential equation (SDE) as a function of a random term $a_2(t)$ given as:

$$U(a_2(t)) = U_{mean} + U_{amp} \times sin(2\pi f_c(a_2(t))), \tag{10}$$

where U_{mean} is the fluctuating mean wind speed, U_{amp} is the amplitude of fluctuation, t is the time, and f_c is the characteristic fluctuating frequency. The random term, $a_2(t)$, sets the state of random characteristic wind speed used to model stochastic phenomenon based on the concept that turbulence is made up of
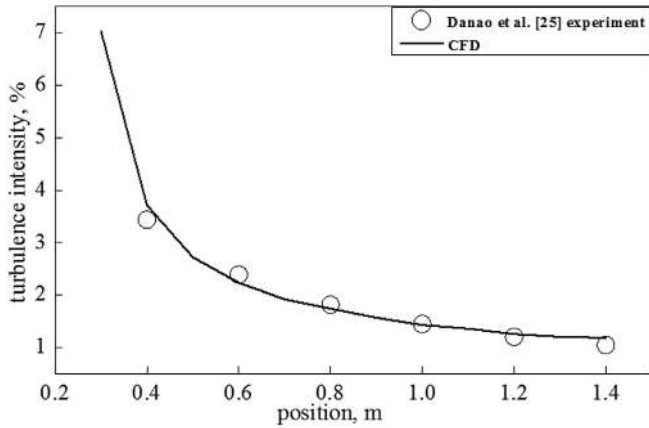
Fig. 4. A comparison of turbulent intensity decay between CFD and experiment.

sinusoidal waves with periods and random amplitudes [66,67].

Stochastic differential equations (SDEs) are widely used to model stochastic phenomena in several fields including building wind speed models. A one-dimensional stochastic differential equation has the general form [68]:

$$dy(t) = a[y(t), t]dt + b[y(t), t]dW(t), \quad t \in [0, T], \tag{11}$$

$$y(0) = y_0, \tag{12}$$

where $a[y(t), t]$ and $b[y(t), t]$ are the drift and the diffusion terms of the SDE, respectively, and $W(t)$ represents a standard Wiener process. This kind of equation can be viewed as an ordinary differential equation where an additional term is included to model the stochastic dynamical behavior related to variable $y(t)$. The standard Wiener process $(W(t), t \in [0, +\infty])$ is a non-stationary diffusion process with the following characteristics [68]:

- $W(0) = 0$, with probability 1.
- The function $t \mapsto W(t)$ is almost surely continuous.
- For $0 \leq t_i < t_{i+1} \leq T$, the random variable defined by the increment $\Delta W_i = W(t_{i+1}) - W(t_i)$ is Gaussian distributed with mean zero and variance $h = t_{i+1} - t_i$, i.e., $\Delta W_i \sim N(0, h)$.
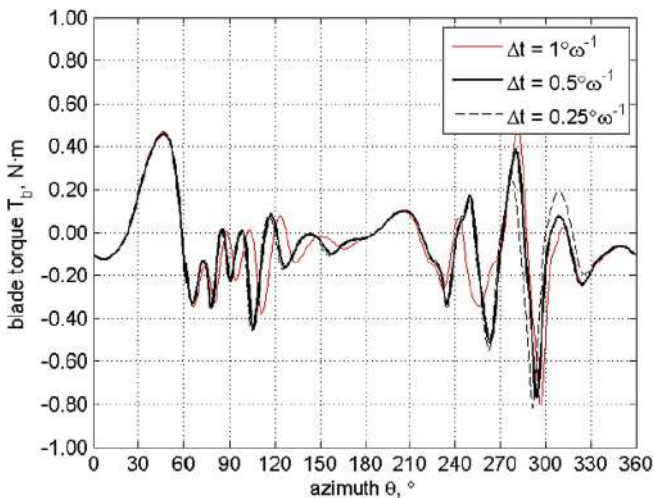

Fig. 5. Time step size study results at $\lambda = 2$ [11,37].

- For $0 \leq t_i < t_{i+1} < t_{i+2} \leq T$, the non-overlapping increments $\Delta W_i = W(t_{i+1}) - W(t_i)$ and $\Delta W_{i+1} = W(t_{i+2}) - W(t_{i+1})$ are independent.

All algorithms were carefully coded and implemented in MAT-LAB R2014b to produce wind velocity fluctuation profiles for the stochastic differential equation (Eq. (10)). For further details, the interested readers are referred to [69] for classical turbulent wind models, in particular the Von Karman Wind Turbulence Model. The stochastic time series wind velocity profiles are compared to those of sinusoidal as can be seen in Fig. 8. A complete understanding of stochastic processes and applications of numerical methods to SDE is beyond the scope and aim of this study and the interested reader is referred to [67,68,70—72], and references therein] for full details.

Following Wekesa et al. [22] numerical model analysis of a VAWT aerodynamics under unsteady wind conditions, Eq. (10) can be simplified and idealized as sinusoidal. With respect to time, the instantaneous inlet velocity $U(t)$ is [22]:

$$U(t) = U_{mean} + U_{amp} \times \sin(2\pi f_c t). \tag{13}$$

In the present study, a fluctuating mean wind speed of $U_{mean} = 11$ m/s with a fluctuating amplitude of $U_{amp} = 4.26$ m/s has been used. This is the unsteady wind characteristics of Marsabit station, a rural-urban town in Eastern Kenya [22,73]. Further details on empirical and numerical analysis of small wind turbine aerodynamic performance and how the unsteady wind characteristics are imposed into the CFD model can be obtained from the authors's previous studies in Refs. [23] and [22], respectively. In order to demonstrate an enhanced wind energy capture, characteristic fluctuation frequencies at $f_c = 0.5$ Hz, 1.0 Hz, and 2.0 Hz have been selected for accurate unsteady wind approximation (Section 4). The velocity profiles are implemented by means of User-Defined Function (UDF) subroutines attached to the solver to control the dynamic mesh motion. The velocity profile fluctuations for all the three f_c cases in Eq. (13) must be obtained using a UDF because the flow solver does not provide these. More details as to how the unsteady wind characteristics are imposed in the model can be found from the previous work by the authors [11,21—24].

3.5. Simulation setup

The coupled pressure-based solver was selected with a second order implicit transient formulation for improved accuracy to solve low-speed incompressible flows. All the governing equations for the solution variables, which are decoupled from each other, are solved sequentially and the SIMPLE algorithm scheme was used to solve the pressure-velocity coupling. With respect to the discretization of the convection terms in the transport equations for the velocity and the turbulence quantities, second-order upwind schemes are utilized [11,50].

The Green-Gauss cell based method was employed for calculating the gradients of the transport quantities on the faces of the cell boundaries. The details of the numerical set-up and imposed under-relaxation factors are reported in Table 3 for easier comparison with other studies. The present simulations required an average of about 20 sub-iterations to make the solution converge at each physical time step. The time step convergence was monitored and the simulation was considered to have converged after 5 rotations of the turbine rotor when residuals of all conserved variables fell below 1×10^{-5} [21—24,46]. This meant that periodic convergence was also achieved [11]. Following studies in Refs. [11,21—23], the simulations were made to run up to ten rotations in each test to ensure reasonable periodic convergence. Similar to the validation preliminary studies by the authors'
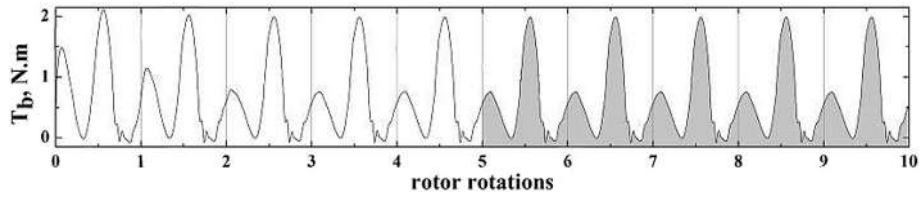
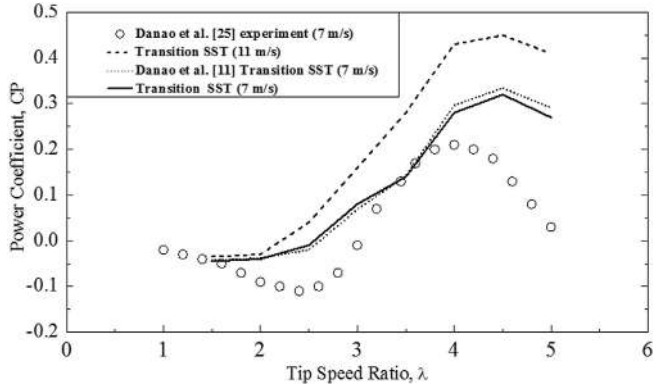**Fig. 6.** Blade torque, (T_b), ripple of one blade for 10 full rotations [21,22].


Fig. 7. Steady power coefficient curves.

previous work in Refs. [21,22] as shown in Fig. 6, the peaks of upwind and downwind torques are irregular for the first five cycles while regularity in the torque peaks is seen after the fifth rotation. A close match in the upwind torque peaks and downwind ripples is seen and hence the simulation is considered converged. Furthermore, there was sufficient inner iterations per time step and each time step was small enough to account for the fluctuations in inflow speed.

The calculations were performed on a computer having, Intel® Core™ i7-2600 CPU@3.40 GHz, 4 cores, 8 threads, physical RAM of 8 GB, and Windows 8 professional 64-bit operating system. A total Central Processing Unit (CPU) run time of about 4 days was required for one unsteady wind condition simulation in all the three f_c cases under study.
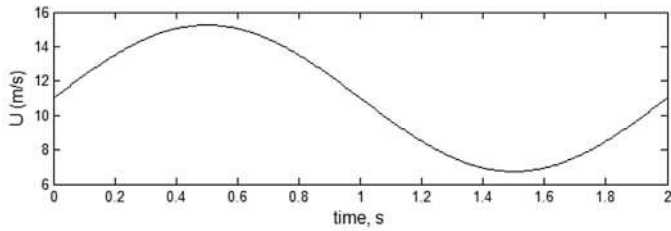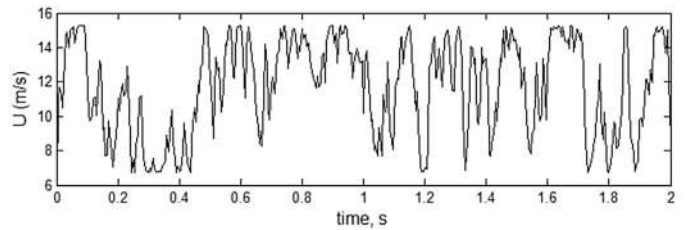

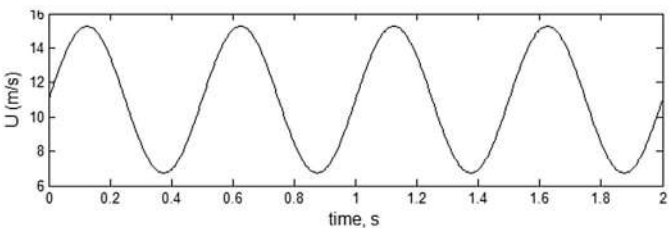(a) Sinusoidal wind velocity at f_c=0.5 Hz
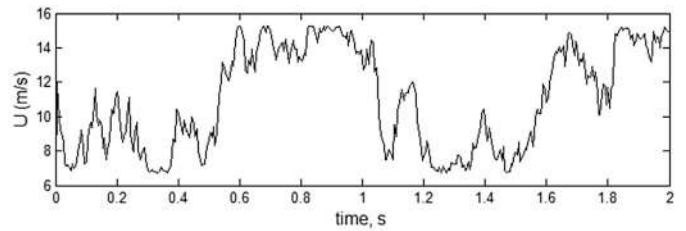
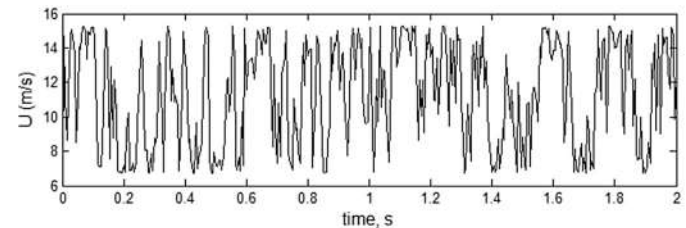(b) Stochastic wind velocity at f_c=0.5 Hz
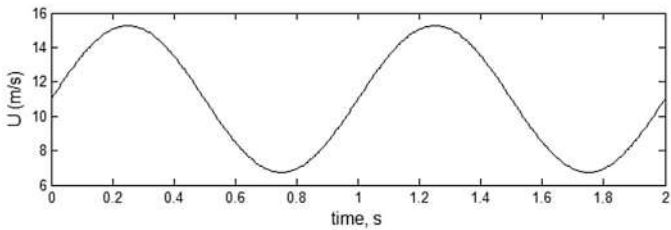
(c) Sinusoidal wind velocity at f_c=1 Hz

(d) Stochastic wind velocity at f_c=1 Hz

(e) Sinusoidal wind velocity at f_c=2 Hz

(f) Stochastic wind velocity at f_c=2 Hz

Fig. 8. Time series for fluctuating wind velocity profiles.

3.6. Turbulence model

The choice of an appropriate turbulence model influences the computational results and the required computation resource because not every model can predict precisely unsteady separation phenomenon [74]. The turbulence of air is treated as an incompressible medium. The Transition Shear Stress Transport (SST) model with the modification suggested by Menter [75,76], and as proposed by Wekesa et al. [21–24], was used for turbulent calculations. This can be attributed to its well behaviour in adverse pressure gradients and separating flow, which were typically seen during the unsteady wind inflow operation on VAWT scales.

Preliminary calculations were also carried out using k-ω Shear Stress Transport (SST) [11,22]. The reason for this choice including validation of the CFD model has been explained in detail by need of comparison with other calculations as reported in the previous work by the authors [11,21,22]. As a result, Transition SST has become a standard for the present calculations and its good applicability for solving flow problems has already been tested in Refs. [11,21–24]. Observe in Fig. 7 that, the Transition SST model gives a good agreement between computational and experimental results.

In addition, previous studies in Refs. [11,14,15,21,22,46,64,76–79] have shown that the Transition SST model was able to simulate in detail and trace experimental results from the literature for positive performance. Detailed explanation for the turbulence model preliminary studies including the assumption made can be obtained in Refs. [11,21,22,64,65,76], and references therein].

4. Results and discussion

In order to resolve a wind rotor flow for enhancing wind energy capture, varying fluctuation frequencies at $f_c = 0.5$, 1.0, and 2.0 Hz were run for accurate unsteady wind approximation and corresponding energy coefficients measured (Table 4).

The variations of tip speed ratio λ with time t for the three f_c cases have a similar minimum and maximum of 3.4 and 7.8, respectively (Fig. 9(a)). Fig. 9(a), 9(b), and 9(c) show lateral compression as f_c increases leading to shorter periods ($t_c=2$ s for $f_c = 0.5$ Hz, $t_c = 1$ s for $f_c = 1$ Hz, and $t_c = 0.5$ s for $f_c = 2$ Hz).

In an effort to present similar amount of spectral data and to provide useful comparative plots for C_e performance for the three f_c cases, the quasi-steady C_e (Fig. 9(c)) is computed from the unsteady C_e (Fig. 9(b)) using smoothing method. Smoothing the unsteady C_e is shown to be consistent with the cycle-averaged method for computing the rotor power performance in steady wind conditions [11,21]. The filtered quasi-steady time series C_e plot (Fig. 9(c)) shows a similar level of unfiltered C_e unsteady plot (Fig. 9(b)) to give a single value prediction of the rotor energy performance.

The C_e variations between f_c cases show very small contraction in the peaks and troughs as f_c increases with maximum C_e decreasing from 0.728, 0.708, to 0.652 for $f_c = 0.5$ Hz, $f_c = 1$ Hz, and $f_c = 2$ Hz, respectively (Fig. 9(c)). While, the minimum C_e changes in increasing values of -0.653, -0.652, and -0.555 for $f_c = 0.5$ Hz, $f_c = 1$ Hz, and $f_c = 2$ Hz, respectively. These changes are considered to be negligible as the cycle-averaged C_e marginally changes from 0.36 when $f_c = 0.5$ Hz to 0.37 for both $f_c = 1$ Hz and $f_c = 2$ Hz cases (Table 4).

Observe in Fig. 9(d) that, the C_e-λ curves are overlapping and coincide each other with very little deviation of the highest f_c case in the high λ region. It can be seen from the figure that maximum steady C_e is 0.45 at optimal tip speed ratio $\lambda^* = 0.45$. In addition, the unsteady C_e of the three f_c cases generally fall within the limits of the steady C_e performance band with fluctuating frequency cases $f_c = 1$ Hz and $f_c = 2$ Hz resulting into 16% drop from the maximum steady C_e (Table 4).

The T_b across different rotor cycles within the first half of the wind cycle for the three f_c cases shows slight variations (Fig. 10). The upwind region across the azimuth positions is associated with large positive T_b for all f_c cases (Fig. 10 sub-graphs). Large positive T_b throughout the upwind with notably high values were produced from $\theta = 60^0$ to $\theta = 130^0$ across the three f_c cases under investigation. The third case, where $f_c = 0.5$ Hz, shows the lowest maximum T_b of 4.41 Nm in cycle 24 (Fig. 10(c)). The cases with $f_c = 2$ Hz and $f_c = 1$ Hz registers maximum T_b values of 6.20 Nm and 6.30 Nm in cycles 1 and 6, respectively (Fig. 10(a) and 10(b)).

The average torque varies significantly for the highest fluctuation frequency case of $f_c = 2$ Hz, as shown in Fig. 10(a) where it is 1.22 Nm for cycle 1, 0.69 Nm for cycle 3, and -0.20 Nm for cycle 6. The average T_b cycle variation for case of $f_c = 1$ Hz is uniform across the cycles where it is 1.26 Nm for cycle 1, 1.27 Nm for cycle 6, and 1.23 Nm for cycle 12 (Fig. 10(b)). The last case with the lowest fluctuation frequency at $f_c = 0.5$ Hz generates average T_b cycle values of 0.38 Nm for cycle 1, 0.29 Nm for cycle 12, and 0.79 Nm for cycle 24 (Fig. 10(c)).

Each point on the energy coefficient C_e curves (Fig. 9(d)) illustrates the ratio of energy extracted to energy available (Eq. (9)), and contains information about how effective the rotor was extracting energy from the entire wind cycle profile. For all the three f_c cases, hysteresis loops in C_e are visible as a result of the unsteady inflow. The C_e curves of the three f_c cases are on top of each other with the hysteresis loop most evident for the fluctuation frequency of 2 Hz in the high λ region. As the frequency of wind fluctuation increases, the rotor starts to encounter the changing wind speed because the rotor frequency is much closer to the wind frequency. The converse is true when the wind fluctuation is slow, the rotor perceives a quasi-steady wind due to the much faster rotor rotation frequency as compared to the wind frequency. At $f_c = 1$ Hz and $f_c = 2$ Hz, majority of the unsteady flow physics is captured across λ resulting in consistent C_e changes with movement along the steady C_e curve.

Uniform positive T_b averages at $f_c = 1$ Hz across the cycles (Fig. 10(b)) demonstrate that the highest frequency of fluctuation with optimal and meaningful energy content in unsteady wind condition is ≈ 1 Hz. As alluded to earlier, the period of the gust under this unsteady condition is equal to 24 rotor revolutions. Since no significant deviation is apparent from the range of variation of the steady energy coefficient, the present study aerodynamic rotor behavior can be deemed quasi-steady. Furthermore, it is noteworthy that the frequency of wind fluctuations studied in the present study is limited to a maximum of 2 Hz since there is no appreciable energy content that can be extracted from higher frequencies as studied by McIntosh [2,13] and Bert'enyi et al. [3], where 99% of the energy content in the wind had a maximum frequency of 1 Hz.

The large positive T_b values evident on the upwind side in Fig. 10 may be attributed to the unperturbed wind and a near static stall that the blade experiences. In the downwind, the high torque generated in the upwind significantly drops and the rotor cycles experiences negative torques across the three f_c cases due the low α experienced by the blade surface.

Consequently, the variation of the energy coefficients that is

Table 4
Wind cycle-averaged C_e at different fluctuation frequencies f_c.

Characteristic fluctuation frequency (f_c)	0.5 Hz	1 Hz	2 Hz
Cycle-averaged energy coefficient (C_e)	0.36	0.37	0.37

(a) Wind cycle fluctuation frequencies

(b) Unsteady C_e across f_c cases

(c) Quasi-steady C_e across f_c cases

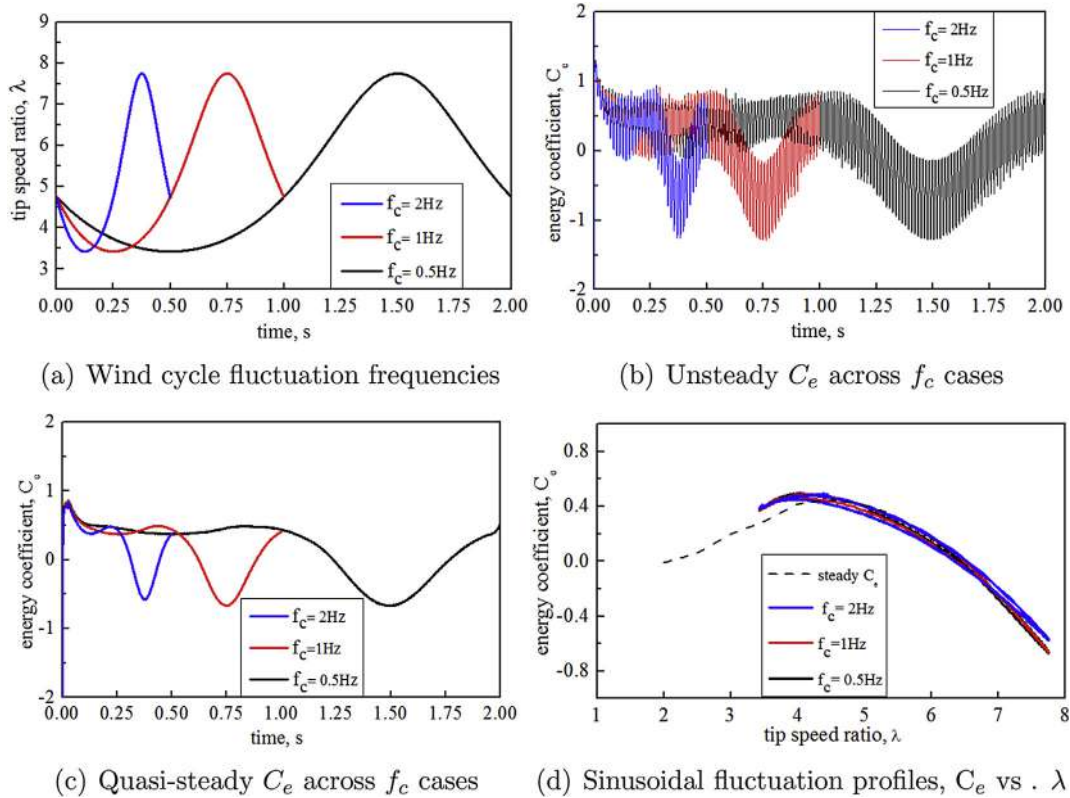(d) Sinusoidal fluctuation profiles, C_e vs . λ

Fig. 9. The effect of varying f_c on energy performance in unsteady wind inflow.

caused by the continuous change in angle of attack on the blades as they revolve is far more significant than that which is induced by the unsteadiness in the wind conditions. Fig. 11 shows flow visualization of vorticity profiles as U_∞ fluctuates across the wind fluctuation cycle for the 1.0 Hz f_c case at $U_{mean} = 11.00$ m/s. Since there was no visible difference between the three blades at the same θ, stalling of one blade at different rotor cycles was monitored. This is attributable to low frequency of the wind speed cycle compared to that of the rotor cycle [11,21,22,45].

As can be seen in Fig. 11, there is no visible flow separation on the blade surface for azimuth position $\theta = 60°$ in all rotor cycles following thin wake. The region is associated with large positive torque as can be observed in Fig. 10(b) for the same wind fluctuation condition at $f_c = 1.0$ Hz. This could be as a result of the stagnation point staying at the trailing edge. From Fig. 11, partial separation can be observed from $\theta = 90°$ in all rotations with visible full separation stall at $\theta = 130°$ in cycle 6. The full separation can be associated with significant negative torque that the blade achieves in cycle 6 as shown in Fig. 10(b). A large negative drop in torque with full separated flow is visible at $\theta = 130°$ in cycle 6 extending to $\theta = 170°$, and even to $\theta = 180°$ (see Fig. 10(b) and Fig. 11).

The vorticity flow field across the rotor cycles in the downwind region shows a similar pattern of re-attachment, and matches the blade torque plot (see Fig. 10(b)) from $\theta = 210°$ to $\theta = 270°$. The re-attachment could be due to the low α experienced by the blade surface. Beyond $\theta = 270°$, T_b drops in magnitude and blades start experiencing negative T_b fluctuation as they complete the rotor cycle (see Fig. 10(b)). Similarly, Wekesa et al. [21,22] attributed this large regions of negative torque in the downwind side to very steep α that the blade experiences at the region inducing persistent large scale vortex shedding.

Generally, for all the three f_c cases, analogous large regions of

negative wind performance and large visible fluctuations in wind speed are revealed by deep stall and large flow separation of vortex shedding. As a result, the shapes of the loops change insignificantly in energy coefficient across the tip speed ratio while the cycle-averaged C_e marginally changes.

Based on unsteady wind researches, and similar to the present study, studies in Refs. [2,3,11–13,21] estimated that the highest fluctuation frequency with meaningful energy content in an urban environment is ≈ 1 Hz. Although there is no control as to what frequencies is expected in the actual field, from the present study, there is the choice of not putting effort to extracting the energy at higher frequencies ($f_c > 1$ Hz); since it has insignificant effect on the total performance of the energy spectrum. That means, the response time of the control system is selected as a design choice considering the frequencies of the changing wind, the rotor mass moment of inertia, the logging frequency of the instrumentation, among others. Therefore, a balance between maximum energy extraction and control system complexity is at the hands of the designer. Hence, if one finds it impractical to extract the remaining 1% of the energy in the turbulent wind as revealed by McIntosh [2,13], one has the control of how the system is designed.

The large positive T_b with consistence values at $f_c = 1$ Hz in the upwind implies that the frequency range is adequate to capture majority of the short periodic fluctuations to represent a length scale for an unsteady urban wind. Furthermore, C_e variations across the three f_c cases are in agreement with unsteady power coefficient analyses studies in Refs. [11,21] where very little deviation of the highest f_c case in the high λ was revealed. In the present study, the differences in the C_e performance are insignificant and can be considered negligible within the test parameters under investigation. As such, efforts on gust tracking and rapid system response could be futile at higher frequencies.
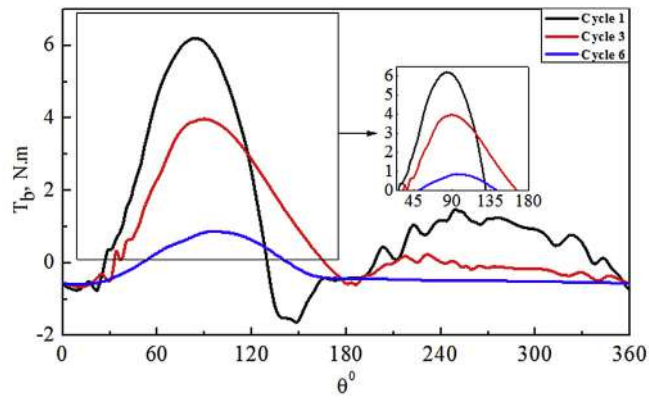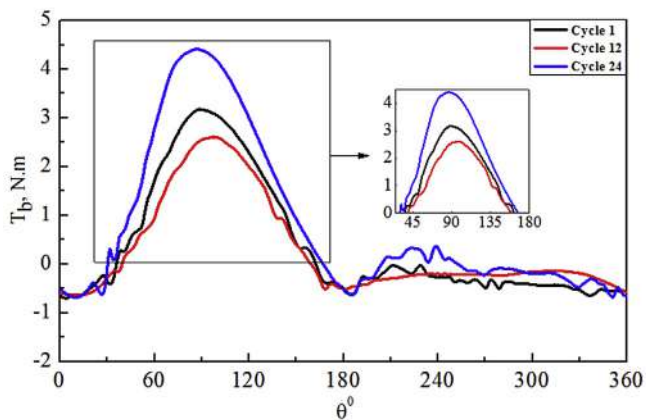
(a) $f_c=2.0$ Hz
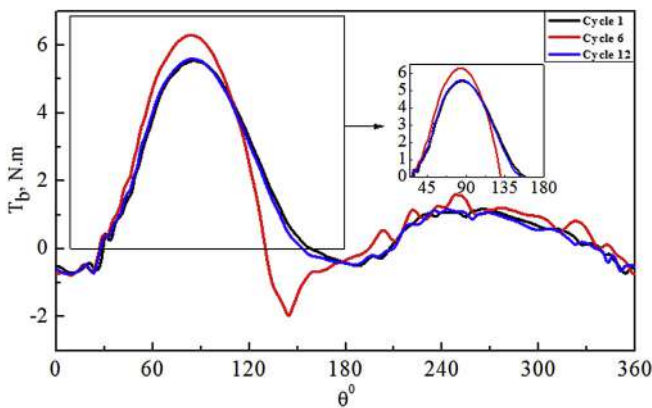
(b) $f_c=1.0$ Hz

(c) $f_c=0.5$ Hz

Fig. 10. Blade torque T_b from three rotor cycles of different f_c cases.

Fig. 11. Vorticity contour profiles for three rotor cycles at $f_c = 1.0$ Hz.

Similar to the present study, using Vorticity transport model, Scheurich and Brown [12] showed that the unsteady energy performance of all the f_c cases generally fell within the limits of the steady power performance band. The revelations in Ref. [12] supports the present study findings that fluctuating wind performance of VAWTs can be tracked and optimized using the uniform wind CP curve. However, at very low fluctuation frequency range, McIntosh et al. [13] presented increased energy performance as f_c increased from 0.05 Hz to 0.5 Hz. This contrasts the present study results at higher frequenc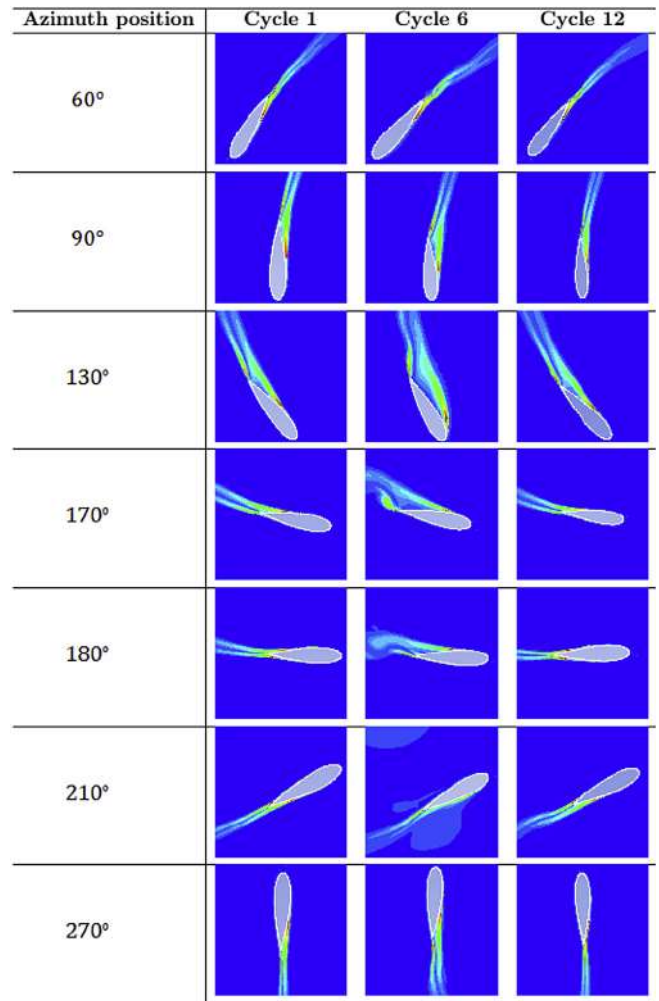ies from 1 Hz to 2 Hz, where insignificant deviation of the energy coefficient performance is evident (Table 4). That means, associated energy performance deviation becomes significant only below low fluctuating frequencies ($f_c < 1$ Hz), whereas high frequencies ($f_c \geq 1$ Hz) of variation in wind speed have a minor effect for practical unsteady wind conditions.

In addition, the effects of different fluctuating frequencies on a wind rotor subjected to unsteady wind were studied in Refs. [14,21]. Similar to the present study, in spite of increased available power, the energy performance degraded over one wind cycle for all unsteady wind f_c cases. In the present work, a 16% drop in cycle-averaged C_e from the steady C_e is obtained for unsteady conditions when $f_c = 1$ Hz and $f_c = 2$ Hz at a fluctuating mean wind speed of $U_{mean} = 11$ m/s with a fluctuating amplitude of $U_{amp} = 4.26$ m/s. It is worth noting that the present numerical approach tries to consider wind velocity fluctuations without assessing topology effects, and that constant wind direction in the model is just an assumption.

5. Conclusion

In this paper, we have proposed a CFD method to analyze wind energy capture on a wind rotor in a fluctuating free-stream. The study presents unsteady calculations using unsteady RANS solver with a developed CFD-based 2D model to demonstrate enhanced wind energy capture.

The CFD results of this investigation show that a hysteresis loop was developed in the energy coefficient variations with tip speed ratio. For all the three f_c cases, the shapes of the loops change insignificantly in energy coefficient across the tip speed ratio while the cycle-averaged C_e marginally changes from 0.36 at 0.5 Hz to 0.37 at both 1 Hz and 2 Hz cases. Therefore, the energy generation from fluctuating wind, theoretically containing higher energy content than uniform wind, is not a practical exercise.

The results show that the highest frequency of the wind fluctuations with meaningful energy content in unsteady wind conditions is of the order of 1 Hz. That implies, rotor associated energy performance deviation becomes significant only at frequencies lower than 1 Hz. Therefore, although there is no control as to what frequencies is expected in the actual field, there is the choice of not putting effort to extracting the energy at higher frequencies.

The employed 2D CFD method provides adequate level for enhanced wind energy capture capability. However, to accurately resolve a full rotor axis fluctuating inflow, further experimental validation, multiple-frequency-component analysis and development would be required in future studies. Furthermore, during sudden wind speed changes, the response time of the wind turbine rotor is essential so that optimum operating condition always governs. The concern is not trying to make the blade profile tolerant to the changes in wind speed but the system to adopt to new condition as fast as possible. These findings shed light towards the energy associated with short-period fluctuations of the unsteady wind resource in urban environment.

Acknowledgements

Nomenclature

c	Blade chord	Δ CP	Change in CP
N	Number of blades	θ	Azimuth position
C_d	Drag coefficient	λ	Tip speed ratio
CP	Power coefficient	C_{mean}	Energy coefficient
C_l	Lift coefficient	λ_{mean}	Mean tip speed ratio
D_g	Gust length	ω	Rotor angular speed
f_c	Fluctuating frequency	ρ	Air density
k_{gust}	Reduced gust frequency	σ	Rotor solidity
n_{rev}	Revolutions per wind cycle	u	Stream-wise velocity component
P_b	Blade power (single blade)	u'	Stream-wise velocity fluctuation
P_B	Blade power (three blades)	u'_{sp}	Short period fluctuations
P_w	Wind power	u'_{lp}	Long period fluctuations
T_b	Blade torque (single blade)	E_{turb}	Total energy extracted from wind
T_B	Blade torque (three blades)	E_{wind}	Total available wind energy
U_∞	Free-stream wind speed	A	Rotor cross-sectional area
R_{rotor}	Rotor radius	SDE	Stochastic Differential Equation
U_{amp}	Fluctuation amplitude from U_{mean}	CFD	Computational Fluid Dynamics
U_{mean}	Mean speed of unsteady wind	VAWT	Vertical Axis Wind Turbine
y^+	Dimensionless wall distance	LES	Large Eddy Simulation
α	Angle of attack	DNS	Direct Numerical Simulations
ω_{mean}	Mean of ω	RANS	Reynolds-Averaged Navier-Stokes

References

[1] Ghadimi P, Rostami AB, Jafarkazemi F. Aerodynamic analysis of the boundary layer region of symmetric airfoils at ground proximity. Aerosp Sci Technol 2012;17:7–20.
[2] Mcintosh S. Wind energy for the built environment. UK: Cambridge University; 2009. p. 105–6. PhD Thesis.
[3] Bertenyi T, Wickins C, McIntosh S. Enhanced energy capture through gust-tracking in the urban wind environment. In: 48th AIAA Aerospace sciences meeting including the new horizons forum and Aerospace exposition, 48. AIAA; 2010. p. 1–7.
[4] Vermeer L, Sorensen J, Crespo A. Wind turbine wake aerodynamics. Prog Aerosp Sci 2003;39:467–510.
[5] Qu Q, Jia X, Wang W, Liu P, Agarwal RK. Numerical study of the aerodynamics of a {NACA} 4412 airfoil in dynamic ground effect. Aerosp Sci Technol 2014;38:56–63.
[6] Zarovy S, Costello M, Mehta A. Experimental method for studying gust effects on micro rotorcraft. J Aerosp Eng 2013;227:703–13.
[7] Frost W, Shahabi A. A field study of wind over a simulated block building (NASA contractor report. National Aeronautics and Space Administration; 1977. NASA CR-2804), Technical Report.
[8] Johnson E, Jacob J. Development and testing of a gust and shear wind tunnel for navs and mavs. In: 47th AIAA Aerospace sciences meeting including the new horizons forum and aerospace exposition. AIAA; 2009. p. 1–16.
[9] Hasma T, Kato S, Ooka R. Analysis of wind-induced inflow and outflow through a single opening using LES and DES. J Wind Eng Ind. Aerodyn 2008;96:6781691.
[10] Jean M, Julian S. An introduction to turbulent flow. Cambridge University Press; 2000.
[11] Danao LA, Edwards J, Eboibi O, Howell R. A numerical investigation into the influence of unsteady wind on the performance and aerodynamics of a vertical axis wind turbine. Appl Energy 2014;116:111–24.
[12] Scheurich F, Brown RE. Modelling the aerodynamics of vertical-axis wind turbines in unsteady wind conditions. Wind Energy 2013;16:91–107.
[13] S. McIntosh, H. Babinsky, T. Bertenyi, Unsteady power output of vertical axis wind turbines operating within a fluctuating free-stream, in: 46th AIAA aerospace sciences meeting and exhibit, Reno, Nevada.
[14] Danao LA, Qin N, Howell R. A numerical study of blade thickness and camber effects on vertical axis wind turbines. Proc Inst Mech Eng Part A J Power Energy 2012;226:867–81.
[15] Howell R, Qin N, Edwards J, Durrani N. Wind tunnel and numerical study of a small vertical axis wind turbine. Renew Energy 2010;35:412–22.
[16] Roh SC, Kang SH. Effects of a blade profile, the Reynolds number, and the solidity on the performance of a straight bladed vertical axis wind turbine. J Mech Sci Technol 2013;27:3299–307.
[17] Bedon G, Castelli MR, Benini E. Optimization of a Darrieus vertical-axis wind turbine using blade element momentum theory and evolutionary algorithm. Renew Energy 2013;59:184–92.
[18] Song Q, Lubitz WD. Design and testing of a new small wind turbine blade. J Sol Energy Eng 2014;136.
[19] Refan M, Hangan H. Aerodynamic performance of a small horizontal axis wind turbine. J Sol Energy Eng 2012;134.
[20] Lee B, Gerontakos P. Investigation of flow over an oscillating airfoil. J Fluid Mech 2004;512:313–41.
[21] Wekesa DW, Wang C, Wei Y, Danao LAM. Influence of operating conditions on unsteady wind performance of vertical axis wind turbines operating within a fluctuating free-stream: a numerical study. J Wind Eng Ind. Aerodyn 2014;135:76–89.
[22] Wekesa DW, Wang C, Wei Y, Kamau JN, Danao LAM. A numerical analysis of unsteady inflow wind for site specific vertical axis wind turbine: a case study for Marsabit and Garissa in Kenya. Renew Energy 2015;76:32–45.
[23] Wekesa DW, Wang C, Wei Y. Empirical and numerical analysis of small wind turbine aerodynamic performance at a plateau terrain Kenya. Renew Energy 2016;90:377–85.
[24] Wekesa DW, Wang C, Wei Y, Zhu W. Experimental and numerical study of turbulence effect on aerodynamic performance of a small-scale vertical axis wind turbine. J Wind Eng Ind. Aerodyn 2016;157:1–14.
[25] Danao LA, Eboibi O, Howell R. An experimental investigation into the influence of unsteady wind on the performance of a vertical axis wind turbine. Appl Energy 2013;107:403–11.
[26] Kim DH, Chang JW. Low-Reynolds-number effect on the aerodynamic characteristics of a pitching NACA 0012 airfoil. Aerosp Sci Technol 2014;32:162–8.
[27] Eboibi O. The influence of blade chord on the aerodynamics and performance of vertical axis wind turbines. UK: The University of Sheffield; 2013. PhD Thesis.
[28] Tanner M. Investigations into incompressible steady base flows. Aerosp Sci Technol 2010;14:126–33.
[29] Barlas T, van Kuik G. Review of state of the art in smart rotor control research for wind turbines. Prog Aerosp Sci 2010;46:1–27.
[30] de Divitiis N. Tait-Kirchhoff method for determining rotary and unsteady force derivatives. Aerosp Sci Technol 2014;39:384–94.
[31] Antoniadis A, Drikakis D, Zhong B, Barakos G, Steijl R, Biava M, et al. Assessment of cfd methods against experimental flow measurements for helicopter flows. Aerosp Sci Technol 2012;19:86–100.

[32] Yang L, Wang M, Gao Z. Numerical investigation of unsteady aerodynamic characteristics of a pitching missile. Aerosp Sci Technol 2010;15:129—36.

[33] Ground C, Maddalena L, Viti V. Numerical analysis and characterization of the dissociated flowfield inside a 1.6 {MW} arc-heated wind tunnel facility. Aerosp Sci Technol 2013;30:306—14.

[34] Mehta D, van Zuijlen A, Koren B, Holierhoek J, Bijl H. Large eddy simulation of wind farm aerodynamics: a review. J Wind Eng Ind. Aerodyn 2014;133:1—17.

[35] Aboshosha H, Bitsuamlak G, El Damatty A. Turbulence characterization of downbursts using les. J Wind Eng Ind. Aerodyn 2015;136:46—61.

[36] Warzecha P, Boguslawski A. LES and RANS modeling of pulverized coal combustion in swirl burner for air and oxy-combustion technologies. Energy 2014;66:732—43.

[37] Wekesa DW. Aerodynamic loading and performance of vertical Axis wind turbines under unsteady winds. P.R. China: Department of Aerospace Engineering and Mechanics. Harbin Institute of Technology; 2016. PhD Thesis.

[38] Barakos GN, Drikakis D. Computational study of unsteady turbulent flows around oscillating and ramping aerofoils. Int J Numer Methods Fluids 2003;42:163186.

[39] Nobile R, Vahdati M, Barlow JF, Mewburn-Crook A. Unsteady flow simulation of a vertical axis augmented wind turbine: a two-dimensional study. J Wind Eng Ind. Aerodyn 2014;125:168—79.

[40] Eboibi O, Danao LA, Howell R, Edwards JM. A numerical study of the influence of blade profile and solidity on the performance of vertical axis wind turbines. In: 51st AIAA aerospace sciences meeting including the new horizons forum and aerospace exposition; 2013.

[41] Sampaio LEB, Rezende ALT, Nieckele AO. The challenging case of the turbulent flow around a thin plate wind deflector, and its numerical prediction by les and rans models. J Wind Eng Ind. Aerodyn 2014;133:52—64.

[42] Kyrkos A, Ekaterinaris JA. Assessment of an unstructured mesh approach for CFD predictions of the NH90 fuselage rotor. Aerosp Sci Technol 2012;19:77—85.

[43] der Hoven IV. Power spectrum of horizontal wind speed in the frequency range from 0.0007 to 900 cycle per hour. J Meteorol 1957;14:160—4.

[44] S. McIntosh, H. Babinsky, T. Bertenyi, Optimizing the energy output of vertical axis wind turbines for fluctuating wind conditions, in: 45th AIAA aerospace sciences meeting and exhibit, Reno, Nevada.

[45] Bausas MD, Danao LAM. The aerodynamics of a camber-bladed vertical axis wind turbine in unsteady wind. Energy 2015;93:1155—64.

[46] Raciti Castelli M, Englaro A, Benini E. The Darrieus wind turbine: proposal for a new performance prediction model based on CFD. Energy 2011;36:4919—34.

[47] Ghoreyshi M, Cummings RM. Challenges in the aerodynamics modeling of an oscillating and translating airfoil at large incidence angles. Aerosp Sci Technol 2013;28:176—90.

[48] Geissler W. A family of {CFD} boundary conditions to simulate separation control. Aerosp Sci Technol 2010;14:494—504.

[49] Biava M, Vigevano L. Simulation of a complete helicopter: a CFD approach to the study of interference effects. Aerosp Sci Technol 2012;19:37—49.

[50] Wang S, Ingham DB, Ma L, Pourkashanian M, Tao Z. Numerical investigations on dynamic stall of low reynolds number flow around oscillating airfoils. Comput Fluids 2010;39:1529—41.

[51] Mortazavi SM, Soltani MR, Motieyan H. A pareto optimal multi-objective optimization for a horizontal axis wind turbine blade airfoil sections utilizing exergy analysis and neural networks. J Wind Eng Ind. Aerodyn 2015;136:62—72.

[52] D'Alessandro V, Montelpare S, Ricci R, Secchiaroli A. Unsteady aerodynamics of a Savonius wind rotor: a new computational approach for the simulation of energy performance. Energy 2010;35:3349—63.

[53] Drikakis D, Hahn M, Mosedale A, Thornber B. Large eddy simulation using high-resolution and high-order methods. Philos Trans R Soc A 2009;373:2985—17.

[54] Hahn M, Drikakis D. Implicit large-eddy simulation of swept-wing flow using high-resolution methods. Am Inst Aeronautics Astronaut 2009;47:618—30.

[55] Becker B, Reyer M, Swoboda M. Steady and unsteady numerical investigation of transitional shock-boundary-layer-interactions on a fan blade. Aerosp Sci Technol 2007;11:507—17.

[56] Wang S, Ingham DB, Ma L, Pourkashanian M, Tao Z. Turbulence modeling of deep dynamic stall at relatively low Reynolds number. J Fluids Struct 2012;33:191—209.

[57] Gharali K, Johnson DA. Numerical modeling of an S809 airfoil under dynamic stall, erosion and high reduced frequencies. Appl Energy 2012;93:45—52.

[58] Ismail MF, Vijayaraghavan K. The effects of aerofoil profile modification on a vertical axis wind turbine performance. Energy 2015;80:20—31.

[59] Consul C, Willden R, Ferrer E, McCulloch M. Influence of solidity on the performance of a cross-flow turbine. In: 8th European wave and tidal energy conference. Uppsala, Sweden, Uppsala; 2009.

[60] Goude A, Ågren O. Simulations of a vertical axis turbine in a channel. Renew energy 2014;63:477—85.

[61] Moshfeghi M, Song YJ, Xie YH. Effects of near-wall grid spacing on SST-k-w model using NREL phase VI horizontal axis wind turbine. J Wind Eng Ind. Aerodyn 2012;107—108:94—105.

[62] Rocha PC, Rocha HB, Carneiro FM, Vieira da Silva M, Bueno AV. k-w SST (Shear Stress Transport) turbulence model calibration: a case study on a small scale horizontal axis wind turbine. Energy 2014;65:412—8.

[63] Danao LA. The influence of unsteady wind on the performance and aerodynamics of vertical Axis wind turbines. The University of Sheffield; 2012. Ph.D. thesis.

[64] Edwards JM, Danao LA, Howell RJ. Novel experimental power curve determination and computational methods for the performance analysis of vertical axis wind turbines. J Sol Energy Eng 2012;134:031008.

[65] McTavish S, Feszty D, Sankar T. Steady and rotating computational fluid dynamics simulations of a novel vertical axis wind turbine for small-scale power generation. Renew Energy 2012;41:171—9.

[66] Rohatgi J, Barbezier G. Wind turbulence and atmospheric stability-their effect on wind turbine output. Renew Energy 1999;16:908—11.

[67] Higham D. The wiener-askey polynomial chaos for stochastic differential equations. Soc Ind. Appl Math 2001;24:619—44.

[68] Zarate-Minamo R, Anghel M, Milano F. Continuous wind speed models based on stochastic differential equations. Appl Energy 2013;104:42—9.

[69] MATLAB Documentation. Von Karman wind turbulence model (continuous). MathsWorks; 2016.

[70] Higham D. An algorithmic introduction to numerical simulation of stochastic differential equations. Soc Ind. Appl Math 2001;43:525—46.

[71] Castino F, Festa R, Ratto C. Stochastic modelling of wind velocities time series. J Wind Eng Ind. Aerodyn 1998;74—76:141—51.

[72] Nfaoui H, Essiarab H, Sayigh A. A stochastic markov chain model for simulating wind speed time series at Tangiers, Morocco. Renew Energy 2004;29:1407—18.

[73] Kamau J, Kinyua R, Gathua J. 6 years of wind data for Marsabit, Kenya average over 14m/s at 100m hub height; an analysis of the wind energy potential. Renew Energy 2010;35:1298—302.

[74] Li C, Zhu S, Xu Y-l, Xiao Y. 2.5D large eddy simulation of vertical axis wind turbine in consideration of high angle of attack flow. Renew Energy 2013;51:317—30.

[75] Menter FR. Review of the Shear-Stress Transport turbulence model experience from an industrial perspective. Int J Comput Fluid Dyn 2009;23:305—16.

[76] Jafari S, Kosasih B. Flow analysis of shrouded small wind turbine with a simple frustum diffuser with computational fluid dynamics simulations. J Wind Eng Ind. Aerodyn 2014;125:102—10.

[77] Li Y, Calisal SM. Three-dimensional effects and arm effects on modeling a vertical axis tidal current turbine. Renew energy 2010;35:2325—34.

[78] Nobile R, Vahdati M, Barlow JF, Mewburn-Crook A. Unsteady flow simulation of a vertical axis augmented wind turbine: a two-dimensional study. J Wind Eng Ind. Aerodyn 2014;125:168—79.

[79] Catalano P, Tognaccini R. RANS analysis of the low-Reynolds number flow around the SD7003 airfoil. Aerosp Sci Technol 2011;15:615—26.